Received: 18 April 2022 | Revised: 26 May 2022 | Accepted: 12 June 2022

DOI: 10.1002/sus2.79

RESEARCH ARTICLE

SusMat WILEY

Tailoring cobalt-free $La_{0.5}Sr_{0.5}FeO_{3-\delta}$ cathode with a nonmetal cation-doping strategy for high-performance proton-conducting solid oxide fuel cells

Yanru Yin[1] | **Hailu Dai**[2] | **Shoufu Yu**[1] | **Lei Bi**[1] | **Enrico Traversa**[3,4]

[1]School of Resource Environment and Safety Engineering, University of South China, Hengyang, Hunan, China

[2]School of Materials Science and Engineering, Yancheng Institute of Technology, Yancheng, Jiangsu, China

[3]School of Materials and Energy, University of Electronic Science and Technology of China, Chengdu, Sichuan, China

[4]Department of Chemical Science and Technology, University of Rome Tor Vergata, Rome, Italy

Correspondence
Lei Bi, School of Resource Environment and Safety Engineering, University of South China, Hengyang 421001, Hunan, China.
Email: lei.bi@usc.edu.cn

Enrico Traversa, School of Materials and Energy, University of Electronic Science and Technology of China, 2006 Xiyuan Rd, Chengdu 611731, Sichuan, China.
Email: traversa@uestc.edu.cn

Funding information
the National Natural Science Foundation of China, Grant/Award Number: 51972183; the Hundred Youth Talents Program of Hunan; the Startup Funding for Talents at University of South China

Abstract

A nonmetal doping strategy was exploited for the conventional $La_{0.5}Sr_{0.5}FeO_{3-\delta}$ (LSF) cathode, allowing high performance for proton-conducting solid oxide fuel cells (H-SOFCs). Unlike previous studies focusing on the utilization of metal oxides as dopants, phosphorus, which is a nonmetal element, was used as the cation dopant for LSF by partially replacing Fe ions to form the new $La_{0.5}Sr_{0.5}Fe_{0.9}P_{0.1}O_{3-\delta}$ (LSFP) compound. The H-SOFC using the LSFP cathode showed a two-fold peak power density as compared to that using the LSF cathode. Both experimental studies and first-principle calculations were used to unveil the mechanisms for the high performance of the LSFP cells.

KEYWORDS

cathode, high performance, nonmetal doping, proton conductor, solid oxide fuel cell

1 | INTRODUCTION

Energy and environmental problems in the current world call for the development of new technologies that can use fuels in a green and efficient way.[1–3] Therefore, different strategies have been proposed,[4,5] and fuel cells that can directly convert chemical energy into electricity have attracted worldwide attention.[6,7] Among the different types of fuel cells, solid oxide fuel cells (SOFCs) have an all-solid-state structure and work at high temperatures

showing unique advantages.[8] The all-solid-state structure avoids the electrolyte leakage problems for other fuel cells, and the high working temperatures make the use of metal oxides instead of noble metals as electrodes feasible, reducing the cost of the fuel cell.[9,10] However, the traditional SOFCs work at very high temperatures (above 800°C), leading to problems in the cell's lifetime.[11] As a result, the development of SOFCs working at intermediate temperatures has become the trend in the past decade in the SOFC community,[12,13] and proton-conducting SOFCs (H-SOFCs) answer this call.[14–16] H-SOFCs can work at intermediate temperatures, as proton-conducting electrolytes have good ionic conductivity and low activation energy.[17–19] However, the decreased working temperature also leads to sluggish cathode reactions, making the development of cathode materials for H-SOFCs necessary.[20] In addition, previous studies have demonstrated that the direct utilization of the cathodes for conventional oxygen-ion conducting SOFCs (O-SOFCs) for H-SOFCs is not a rational choice, and some high-performing cathodes for traditional SOFCs did not show similar encouraging performance for H-SOFCs,[21] suggesting that the design for H-SOFC cathodes needs further improvement.[22]

Some high-performing cathode materials have been developed in recent years.[23–25] These cathode materials have one common feature: cobalt is one of the major elements in the cathode. This is the same for O-SOFCs as cobalt-containing cathodes show good catalytic activities, boosting the cell performance. However, it is recognized that cobalt-containing cathodes suffer from a few problems, such as thermal mismatch and cobalt evaporation,[26] which need to be addressed for practical applications. In contrast, ferrite-based cathodes have been proposed for H-SOFCs due to their good thermal and chemical compatibility with proton-conducting electrolytes.[27] However, the low fuel cell performance compared with other cathodes makes the application of ferrites not so popular for H-SOFCs. Recently, several studies showed that the performance of ferrite cathodes can be enhanced with proper cation tailoring.[28,29] Therefore, it is reasonable to assume that the performance of traditional ferrite cathodes may challenge the existing high-performing cathodes if suitable dopants are exploited. It has been noted that the doping strategy is the most employed strategy to tailor the cathode materials, allowing it to show desirable performance for SOFCs. Up until now, the current doping strategy for H-SOFC cathodes mainly relies on the use of metal cations, particularly with the transition metal elements.[30] The features of the d-orbital in transition metals allow enhanced properties by doping. To the best of our knowledge, nonmetal cation dopant has not been used for H-SOFC cathodes. However, some nonmetal dopants have been used for O-SOFCs. The boron element can improve the catalytic activity and stability of $La_{0.6}Sr_{0.4}Co_{0.8}Fe_{0.2}O_3$.[31] The P-doping method can boost the performance of bismuth ferrite-based cathode for O-SOFCs.[32] These results imply that the performance of nonmetal-doped cathodes may work well for H-SOFCs, despite the cathode reaction mechanism for O-SOFCs and H-SOFCs are not entirely the same. To demonstrate this hypothesis, $La_{0.5}Sr_{0.5}FeO_{3-\delta}$ (LSF), which is a first-generation cathode for SOFCs and reported to show only moderate performance for H-SOFCs, is used as a case study. The nonmetal element phosphorus was used as the dopant to partially replace Fe ions in LSF to form the $La_{0.5}Sr_{0.5}Fe_{0.9}P_{0.1}O_{3-\delta}$ (LSFP) material. The SOFC performance using LSF with and without P-doping was compared, and the mechanism for the performance enhancement of the LSFP cathode was revealed.

2 | RESULTS AND DISCUSSION

The LSFP material was synthesized using a wet chemical route. Figure 1A shows the X-ray diffraction (XRD) pattern for the LSFP powder. A single phase was obtained for LSFP without any detectable impurities. Compared with the P-free LSF sample, the peaks for LSFP shifted to higher angles due to the smaller ionic radius of P ions (44 pm for P^{3+} and 38 pm for P^{5+}) compared with that for Fe ions (78 pm for Fe^{2+} and 64.5 pm for Fe^{3+}), suggesting the incorporation of P into the LSF lattice. In addition, no phase change could be observed for the LSFP powder from room temperature to 700°C, as detected by the high-temperature in situ XRD (Figure S1), suggesting a good thermal stability for the LSFP material. The reduction in the d-spacing value for the (110) plane observed in Figure 1B,C by using the high-resolution transmission electron microscopy (HR-TEM) for LSF after P-doping also indicates a lattice shrinkage, in agreement with the XRD results. The scanning TEM (STEM) mapping results shown in Figure 1E indicate that the doping of P into LSF did not lead to any elemental segregation, and there is a homogenous distribution of each element, including La, Sr, Fe, and P. All these findings suggest the successful incorporation of P in the LSF lattice. The elemental analysis by scanning electron microscope energy-dispersive X-ray spectroscopy (SEM-EDS) shown in Figure S2 indicates that the atomic ratio of P element to the total cation ions is about 5.3%, which is close to the nominal ratio of P to the total cations (5%), suggesting there is no significant P evaporation for LSFP during the synthesis procedure. Considering EDS is a semi-quantitative method, the inductive coupled plasma emission spectrometer (ICP) method is further used to investigate the P content after firing. The result indicates that the P ratio to the total cation ions is

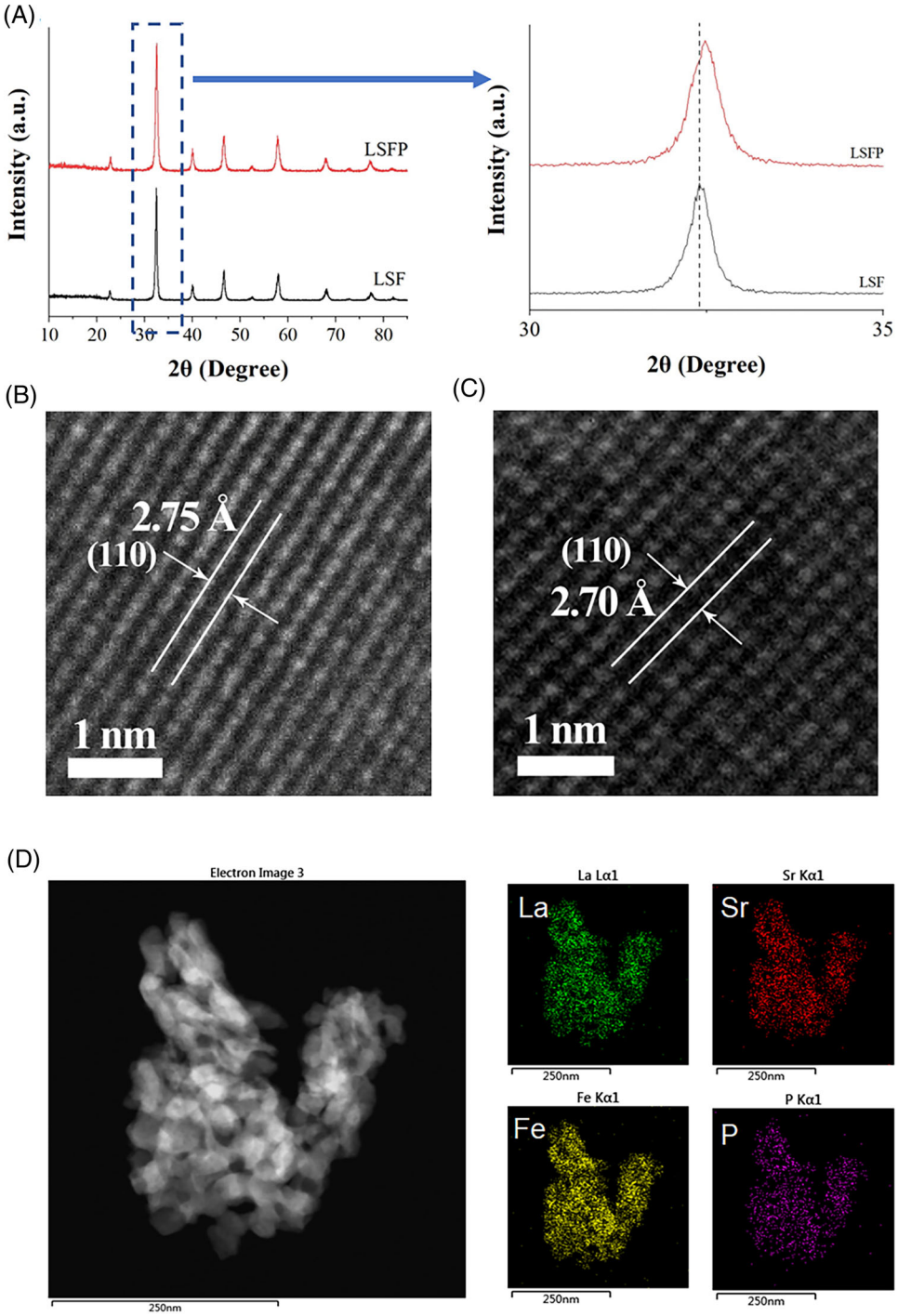

FIGURE 1 (A) X-ray diffraction (XRD) patterns for the synthesized $La_{0.5}Sr_{0.5}FeO_{3-\delta}$ (LSF) and $La_{0.5}Sr_{0.5}Fe_{0.9}P_{0.1}O_{3-\delta}$ (LSFP) powders. High-resolution transmission electron microscopy (HR-TEM) for (B) LSF and (C) LSFP. (D) Elemental mapping of the LSFP powder by scanning TEM (STEM)

about 4.45%, which is close to the nominal value (5%), with only a slight deviation. All this evidence indicates that the evaporation of P could be minor, if there is any. The relatively low calcination temperature of 800°C used in this study could be a reason for retaining the P element in the oxide. This calcination temperature is much lower than that used for the synthesis of other P-containing oxides in the literature,[4,32] and no obvious P evaporation has been reported in those previous studies. Comparing the morphologies of LSF before and after P-doping, there is not much difference in the overall morphology for the powders, as shown in Figure S3A,B. However, the TEM images (Figure S3C,D) of the powders indicate that the average particle size for LSF and LSFP is around 90 and 50 nm,

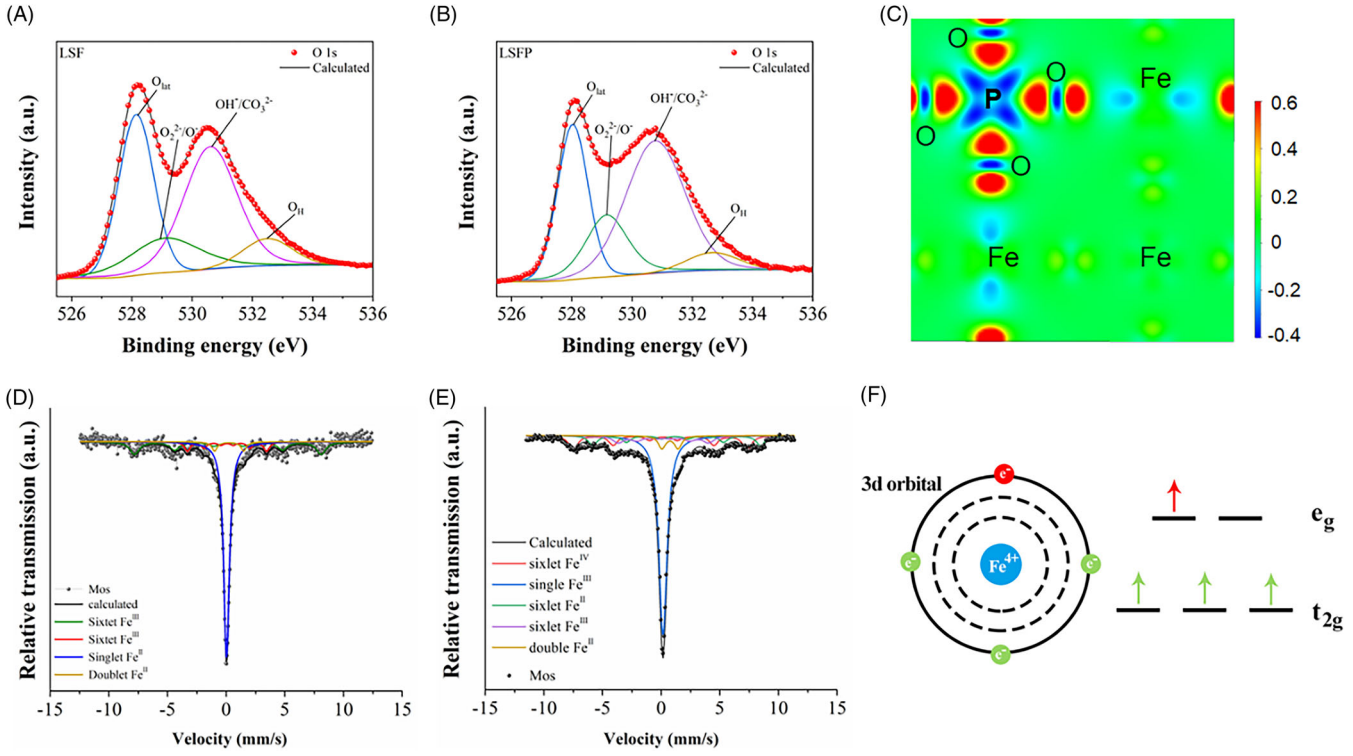

FIGURE 2 X-ray photoelectron spectroscopy (XPS) O 1s curves for (A) $La_{0.5}Sr_{0.5}FeO_{3-\delta}$ (LSF), and (B) $La_{0.5}Sr_{0.5}Fe_{0.9}P_{0.1}O_{3-\delta}$ (LSFP). (C) Charge density difference for LSF after P-doping. [57]Fe Mössbauer spectra for (D) LSF and (E) LSFP. (F) Scheme for the degeneration of the Fe 3d orbital

respectively, suggesting the doping of P restricts the growth of the particle size.

The limitation of traditional LSF for H-SOFCs is due to its moderate catalytic activity at intermediate temperatures.[27] The moderate activity of LSF as a cathode can be anticipated from the atomic level analysis by density functional theory (DFT) calculations, as LSF has a high oxygen vacancy formation energy (E_{vo}), reaching 1.68 eV. In contrast, the E_{vo} for LSFP is lowered to 1.02 eV, suggesting that the formation of oxygen vacancies (Vo) become easier with the P-doping, and Vo might be more abundant for LSFP compared with LSF. The calculation of E_{vo} was achieved by using the equation: $E_{vo} = E_{defect} + \frac{1}{2}E_{O_2} - E_{bulk}$, in which E_{defect} means the energy of a defective bulk, E_{bulk} means the energy of a perfect bulk. The increase in Vo concentration was also demonstrated using X-ray photoelectron spectroscopy (XPS) analysis, as shown in Figure 2A,B. The ratio between the oxygen species related to the surface oxygen vacancies (O_2^{2-} or O^-) and the lattice O (O_{lat}) reflects the oxygen vacancy content of the material,[33–35] and this ratio increased from 0.48 for LSF to 0.63 for LSFP, suggesting the increased surface Vo amount for LSF after P-doping. Vo is important not only for protonation[36] but also for oxygen migration.[37] In addition, it was reported that the Vo-rich surface could be beneficial for the improvement of the catalytic activity,[38–41] which is critical for cathode performance. On the contrary, the hydration energy (E_{hydra}), which is calculated according to the equation:$E_{hydra} = E_{2OH} - E_{defect} - E_{H_2O}$ (E_{2OH} represents the energy of a perfect structure with two additional H atoms), followed an opposite trend: the E_{hydra} increased from −0.68 eV for LSF to 1.01 eV for LSFP, suggesting that hydration is more favorable in LSF. However, a relatively poor proton migration behavior was detected for LSF, 1.52 eV. In contrast, the barrier is reduced to 1.19 eV for LSFP, suggesting that proton migration in LSFP encounters a lower barrier compared with that in LSF, and thus in principle, improved proton transportation could be achieved for LSFP. The lower E_{hydra} for LSF might be counterbalanced by its larger E_{vo} and higher proton migration barrier, making it less advantageous compared with LSFP. Further to the improvement in bulk properties, the surface catalytic activity toward O_2 would be another important parameter as the oxygen reduction reaction (ORR) ability is a critical parameter for the cathode performance.[42,43] Before studying the surface properties, the selection of proper surface terminals is carried out. There are two surface terminals: one is the Fe–O–P terminal and the other is the Fe–O–Fe terminal. It has been calculated that the Fe–O–P terminal has lower surface energy than the Fe–O–Fe terminal, which means it is more stable and has a higher

possibility of exposing at the surface. Therefore, the Fe–O–P terminal is selected for the surface calculations. There are two different sites for the O_2 adsorption at the LSFP surface. One is at the Fe site next to the P cation (Fe–P site), and the other is at the Fe site far from the P cation (Fe–Fe site), as shown in Figure S4. The O_2 adsorption energies were calculated at 0.27 and 0.52 eV on the Fe–P and Fe–Fe sites, respectively, implying O_2 adsorption on the Fe–P site is more favorable at the LSFP surface due to the lower energy.[44–46] The analysis of the charge density difference (Figure 2C) revealed that the P-doping into LSF evidently changes the electronic structure of the Fe ions next to the P cation (Fe–P site), leading to a charge depletion for the Fe ions. The charge depletion could result in the increase of the Fe valence (loss of electrons). In contrast, the Fe ion far from the P cation (Fe–Fe site) receives much less evident influence on the electronic charge. The change in the electronic structure could be the key to the lower O_2 adsorption energy at the Fe–P site. The Mössbauer spectroscopy was utilized to analyze the valence of the Fe ions in both LSF and LSFP. Although Fe^{2+} and Fe^{3+} can be observed in LSF and LSFP, Fe^{4+} is absent from LSF and can only be detected in LSFP, as shown in Figure 2D,E. However, it should be mentioned that although Fe^{4+} can only be detected in LSFP at the Mössbauer spectroscopy, this evidence cannot exclude the existence of the Fe^{4+} in LSF due to high-vacuum testing condition for the Mössbauer spectroscopy, especially considering the high Sr content that possibly leads to the formation of Fe^{4+}.[7] However, the results of the Mössbauer spectroscopy implies the increase in Fe^{4+} content for LSFP as the signal of Fe^{4+} is more evident compared with LSF, which agrees with the previous report that P can induce the formation of Fe^{4+} in $LaFeO_3$.[47] To further investigate the charge change after P-doping, Bader charge analysis with the DFT method is employed to study the effective charge of Fe cations in LSF and LSFP. It is found that the effective charge of Fe ions in LSF is ~1.69 e. In contrast, the effective charge of Fe ions in LSFP is between ~1.71 e and ~1.67 e, in which some Fe ions have higher valence and some have lower valence than that in LSF. Therefore, it is reasonable to have increased Fe^{4+} content in LSFP. In addition, the ICP measurement suggests that there is probably a minor P evaporation, which may also cause the increased Fe^{4+} content due to charge compensation. The Fe^{4+} is reported to be important for the ORR activity of the catalyst, as there is one electron at the e_g orbital as schemed in Figure 2F that tends to give the electron to break the O–O bond.[47] It has been reported that the high e_g orbital filling would lead to a weak interaction between the Fe–O_2, and the best electrocatalytic activity is achieved with e_g filling around one.[48] The formation of Fe^{4+} induced by P-doping could be crucial for the catalytic activity of the cathode. The better catalytic activity of LSFP is demonstrated by the improved interaction between the catalyst and O_2. In contrast to the relatively high O_2 adsorption energy of 1.9 eV at the LSF surface, the O_2 adsorption energy at the LSFP surface is reduced to 0.27 eV, which means that O_2 adsorption has to overcome a lower energy barrier on the LSFP surface as compared with LSF. In addition, the adsorbed O_2 has a larger O–O bond length on LSFP surface (125.5 pm) than that on LSF surface (125.1 pm). Both values are larger than that for O_2 before adsorption (123.2 pm).[28] The enlarged O–O bond length suggests a weaker O–O bond, which could facilitate the ORR. The lower O_2 adsorption energy and enlarged O–O bond length for the adsorbed molecular O_2 indicate an improved interaction between the LSFP catalyst with O_2 as compared with LSF. Therefore, it is reasonable to assume that the LSFP cathode would deliver improved fuel cell performance in the H-SOFC application.

The LSFP and LSF were evaluated as the cathode for H-SOFCs, using $BaCe_{0.7}Zr_{0.1}Y_{0.2}O_{3-\delta}$ (BCZY) as the electrolyte and NiO-BCZY as the anode. The LSF (or LSFP) was mixed with $BaZr_{0.8}Y_{0.2}O_{3-\delta}$ (BZY) proton-conducting oxide to form a composite cathode. BZY instead of BCZY was used as the proton-conducting phase in the composite cathode as the poor sinterability of BZY could restrict the grain growth of the whole composite cathode, leading to higher porosity cathode and smaller particle sizes.[14] Figure 3A indicates that the LSFP cell shows peak power densities of 634, 978, and 1322 mW cm^{-2} at 600°C, 650°C, and 700°C, respectively, which are significantly larger than that for LSF cell (Figure 3B), being 310, 473, and 613 mW cm^{-2} at 600°C, 650°C, and 700°C, respectively. The improvement at each testing temperature is above 100%, as shown in Figure 3C. As both LSFP and LSF cells use identical BCZY/NiO-BCZY half cells, the considerable difference in the fuel cell performance should primarily come from the different cathode catalysts used. The microstructure shown in Figure 3D,E further indicates that both cells have a similar cell structure, with a similar electrolyte thickness of 12.9 μm for the LSFP cell and 13.2 μm for the LSF cell. Therefore, the improved fuel cell performance is due to the material's properties rather than the microstructure.

The electrochemical impedance spectroscopy (EIS) plots for LSF and LSFP cells shown in Figure 3F indicate an obvious reduction in the polarization from the LSF cell to LSFP cell. The EIS plots can be fitted with the equivalent circuit, and three depressed semicircles, which present three different electrochemical reactions, can be found. The high-frequency resistance (R_{HF}), attributable to the charge-transfer process,[22] is similar for both cells, being 0.0155 and 0.0165 Ω cm^2 for the LSF and LSFP cells, respectively. The close R_{HF} values for both cells are expected as the lower proton migration barrier in LSFP might be

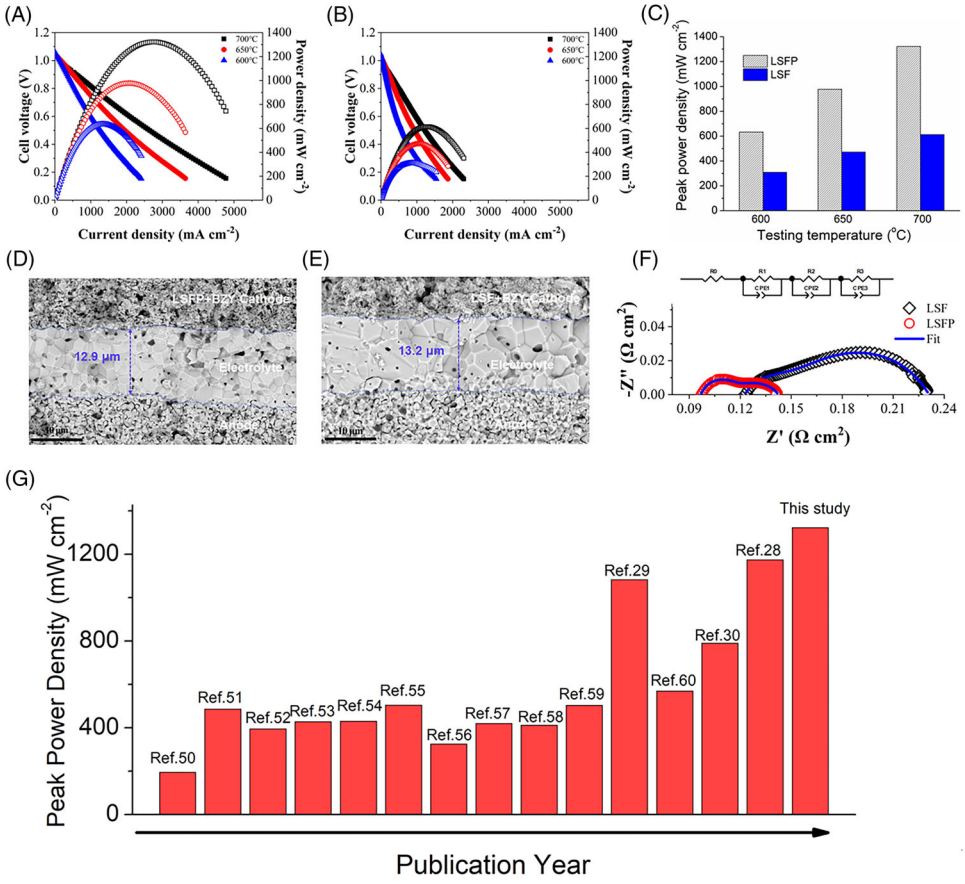

FIGURE 3 IV and power density curves for the cell using (A) LSFP-BZY cathode, and (B) LSF-BZY cathode. (C) Comparison of peak power densities for the $La_{0.5}Sr_{0.5}FeO_{3-\delta}$ (LSF) and $La_{0.5}Sr_{0.5}Fe_{0.9}P_{0.1}O_{3-\delta}$ (LSFP) cells measured at different temperatures. Cross-sectional views for the (D) LSFP cell, and (E) LSF cell. (F) Electrochemical impedance spectroscopy (EIS) plots for LSF and LSFP cells. The hollow symbols are the measured data and the solid lines are the fitted results. The equivalent circuit used to fit the EIS plots is also shown. (G) The comparison of fuel cell performance of the H-SOFCs using ferrite-based cathodes tested at 700°C. Ref.50: $La_{0.7}Sr_{0.3}FeO_3$; Ref.51: $Ba_{0.5}Sr_{0.5}Zn_{0.2}Fe_{0.8}O_3$; Ref.52: $BaCe_{0.5}Fe_{0.5}O_3$; Ref.53: $SrFe_{0.9}Sb_{0.1}O_3$; Ref.54: $Ba_{0.5}Sr_{0.5}Fe_{0.8}Cu_{0.2}O_3$; Ref.55: $Sm_{0.5}Sr_{0.5}Fe_{0.8}Cu_{0.2}O_3$; Ref.56: $Ba_{0.95}La_{0.05}FeO_3$; Ref.57: $Ba_{0.5}Sr_{0.5}Fe_{0.9}Mo_{0.1}O_3$; Ref.58: $La_{0.6}Sr_{0.4}Fe_{0.9}Cr_{0.1}O_3$; Ref.59: $La_{0.6}Sr_{0.4}Fe_{0.9}Nb_{0.1}O_3$; Ref.29: $La_{0.35}Pr_{0.15}Sr_{0.5}FeO_3$; Ref.60: $Pr_{0.5}Sr_{0.5}FeO_3$; Ref.30: $Sr_2Fe_{1.5}Mo_{0.4}Zr_{0.1}O_6$; Ref.28: $La_{0.5}Sr_{0.5}Fe_{0.9}Mo_{0.1}O_3$

balanced by the relatively higher hydration energy compared with LSF, leading to a similar charge-transfer process. Compared with the similar R_{HF}, the middle-frequency (R_{MF}) and low-frequency resistance (R_{LF}) showed huge differences. The R_{MF} and R_{LF} for the LSF cell were 0.0182 and 0.0735 Ω cm^2, respectively. In contrast, R_{MF} and R_{LF} for the LSFP cell were 0.005 and 0.0233 Ω cm^2, respectively, which are significantly reduced when compared with those for the LSF cell. It has been reported that the R_{MF} and R_{LF} represent the oxygen-ion diffusion and O_2 transportation process,[22,49] respectively. The reduction in R_{MF} and R_{LF} in LSFP agrees with the DFT calculations, which showed that lower oxygen vacancy formation energy and improved O_2 adsorption are obtained with LSFP. Compared with the big difference in R_p, ohmic resistance (R_o) of these two cells are close, although some difference can still be observed. As both cells have a similar electrolyte thickness and anode composition, the slightly reduced R_o for the LSFP cell is probably from the improved contact between the cathode and electrolyte due to the smaller particle size of LSFP. Further to the much higher performance than the LSF cell in this study, to the best of our knowledge, the current LSFP cell shows the highest performance compared with other ferrite-based cathodes for H-SOFCs,[28–30,50–60] as indicated in Figure 3G. In a broad context, cobalt-free materials instead of only ferrites are proposed in recent years, aiming to find alternatives for traditional high-performing cathodes containing cobalt element. To achieve high performance, new cobalt-free materials and microstructure optimization strategies are proposed.[61,62] It is noted that even compared with these high-performing cobalt-free cathodes,[63–65] the current LSFP cell shows one of the largest fuel cell outputs, despite the LSFP material being directly used without further microstructure optimizations. Further comparing the performance with other H-SOFCs using cobalt-containing

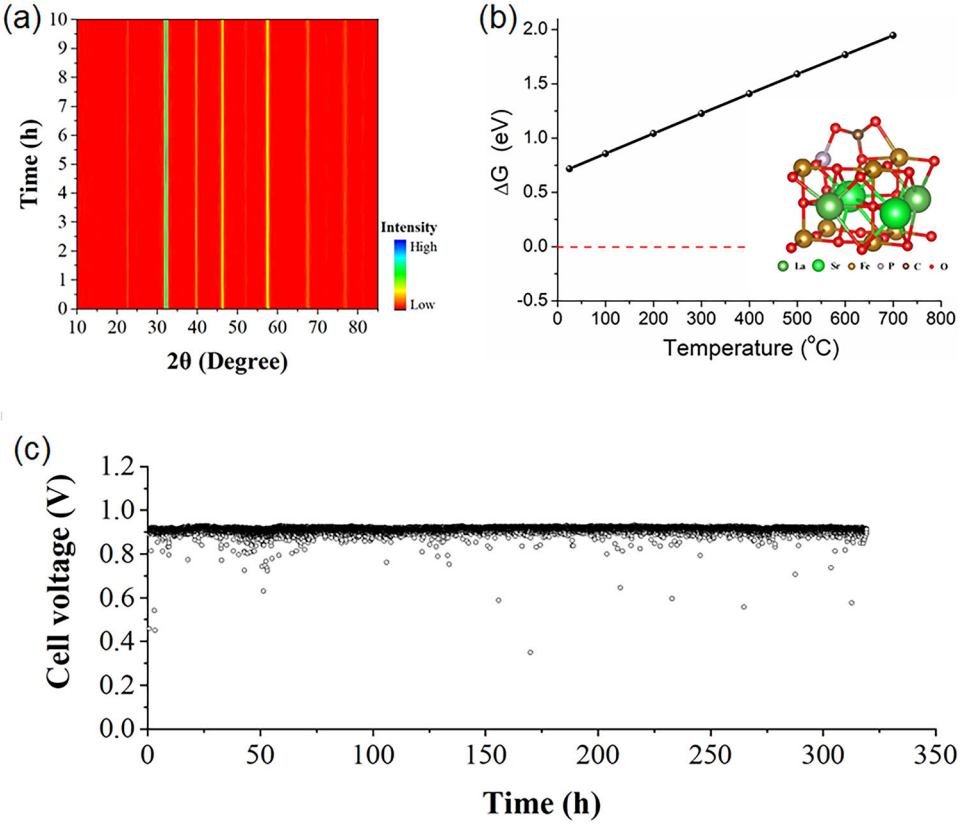

FIGURE 4 (A) Time course of the X-ray diffraction (XRD) patterns for the $La_{0.5}Sr_{0.5}Fe_{0.9}P_{0.1}O_{3-\delta}$ (LSFP) powder measured at 700°C in the CO_2-containing atmosphere. (B) The calculated Gibbs free energy for the possible reaction between LSFP and CO_2 as a function of temperature. The calculated configuration of the CO_2-adsorbed LSFP surface is also shown. (C) Long-term stability of the LSFP cell tested at 600°C with an applied current density of 200 mA cm^{-2}

cathodes, the current LSFP shows higher performance than many of the H-SOFCs reported in the literature and is only inferior to a few reports.[25,66] However, the absence of cobalt element in the cathode avoids the problems in thermal expansion mismatch and cobalt evaporation, making LSFP a promising cathode candidate for H-SOFCs.

In addition to the electrochemical performance, LSFP possesses good chemical stability that can be demonstrated in both experimental studies and first-principle calculations. The LSFP powder was put in a CO_2-containing atmosphere (10 CO_2 + 90% air), and the in situ high-temperature XRD was used to record the phase of the powder as a function of time, as shown in Figure 4A. It is observed that no detectable secondary phases could be found during the whole testing period, suggesting good chemical stability of LSFP against CO_2. First-principle calculations indicate that the Gibbs free energy for the reaction between CO_2 and LSFP is above zero even at room temperature and ΔG increases as a function of the temperature, as shown in Figure 4B. This result indicates that the interaction between CO_2 and LSFP is unfavorable, and LSFP is thermodynamically stable against CO_2 at the fuel cell working temperatures. The excellent stability of LSFP is further demonstrated in the fuel cell working condition, as shown in Figure 4C. The H-SOFC using the LSFP cathode works stably for more than 300 h without noticeable degradations, suggesting good chemical stability and material compatibility of LSFP.

3 | CONCLUSIONS

A nonmetal cation-doping strategy was utilized for the first time to tailor the traditional LSF cathode for H-SOFCs. P cations can partially occupy the Fe site at LSF to form the LSFP material, leading to an apparent electronic change for the neighboring ions. The high catalytic activity of the LSFP catalyst, which doubled the performance of the H-SOFC compared with the one with the traditional LSF. The performance of the LSFP cell is also one of the highest ever reported for the cobalt-free cathodes for H-SOFCs. In addition, the high performance integrates well with excellent chemical stability, suggesting that the nonmetal cation-doping strategy could be an interesting direction for the design of high-performing cathodes for H-SOFCs, although no such attempt was made before this study.

4 | EXPERIMENTAL SECTION

LSFP was prepared by a traditional wet chemical method and the preparation details can be found in our previous reports.[67] It should be noted that ammonium phosphate dibasic was used as the P source in the synthesis. The LSFP precursor was calcined at 800°C for 3 h to reach a single phase. For comparison, the traditional LSF without P-doping was prepared in the same way. The phase purity of the powders was examined by XRD. HR-TEM (JEM-2100F) coupled with EDS was used to analyze morphologies of the samples as well as the elemental distributions. XPS analysis for LSFP and LSF samples was carried out by using a Thermo Fisher ESCALAB 250Xi spectrometer. Mössbauer spectroscopy measurements of LSFP and LSF were performed using a Mössbauer spectroscope (Wissel MS-500). The stability test for LSFP was carried out by putting the LSFP powder in a high-temperature XRD chamber under a flowing 10% CO_2 atmosphere. The flowing rate was set at 30 ml min^{-1}. XRD patterns for the LSFP powder at 600°C under such a condition were recorded as a function of time.

Half-cells using the BCZY electrolyte and NiO-BCZY anode were prepared, and the fabrication details can be found elsewhere.[68] LSFP (or LSF) powder was mixed with BZY powder in a weight ratio of 7:3, forming the composite cathode powder. Then the composite cathode was deposited on the sintered BCZY electrolyte surface, followed by a co-sintering procedure in a microwave furnace at 800°C for 10 min, forming the complete cell. Complete cells were tested in the fuel cell working condition using H_2 as the fuel. The electrochemical performance of the cells was recorded with an electrochemical workstation (Squidstat Plus, Admiral Instrument). The RelaxIS software was used to fit the impedance plot of the cell.

Theoretical calculations were carried out by using the DFT method[69] with the VASP (Vienna ab initio simulation package)[70] software with the Perdew, Burke, and Ernzerhof (PBE)[71] exchange correlation potential within the generalized gradient approximation (GGA).[72] All calculations were performed with a cutoff energy for the valence electrons of 500 eV, in a (4 × 4 × 4) gamma-centered K-point mesh. The calculation details can be found in our previous studies.[23,73]

ACKNOWLEDGMENTS

This work was supported by the National Natural Science Foundation of China (Grant Number: 51972183), the Hundred Youth Talents Program of Hunan, and the Startup Funding for Talents at University of South China.

CONFLICT OF INTEREST

The authors declare no conflict of interest.

DATA AVAILABILITY STATEMENT

The data that support the findings of this study are available from the corresponding author upon reasonable request.

ORCID

Lei Bi https://orcid.org/0000-0001-9479-0776

REFERENCES

1. Mei J, Liao T, Liang J, Qiao YX, Dou SX, Sun ZQ. Toward promising cathode catalysts for nonlithium metal-oxygen batteries. *Adv Energy Mater*. 2020;10(11):1901997.
2. Zhang YW, Mei J, Yan C, Liao T, Bell J, Sun ZQ. Bioinspired 2D nanomaterials for sustainable applications. *Adv Mater*. 2020;32(18):1902806.
3. Li QF, Chen HL, Lv X, et al. Advances in metal phosphides for sodium-ion batteries. *SusMat*. 2021;1(3):359–392.
4. Liu JP, Wang J, Belotti A, Ciucci F. P-substituted $Ba_{0.95}La_{0.05}FeO_3$ as a cathode material for SOFCs. *ACS Appl Energy Mater*. 2019;2(8):5472–5480.
5. Irvine J, Rupp JLM, Liu G, et al. Roadmap on inorganic perovskites for energy applications. *J Phys Energy*. 2021;3(3):031502.
6. Brett DJL, Atkinson A, Brandon NP, Skinner SJ. Intermediate temperature solid oxide fuel cells. *Chem Soc Rev*. 2008;37(8):1568–1578.
7. Li M, Wang Y, Wang YL, Chen FL, Xia CR. Bismuth doped lanthanum ferrite perovskites as novel cathodes for intermediate-temperature solid oxide fuel cells. *ACS Appl Mater Interfaces*. 2014;6(14):11286–11294.
8. Zhao K, Hou XX, Norton MG, Ha S. Application of a NiMo-$Ce_{0.5}Zr_{0.5}O_2$ catalyst for solid oxide fuel cells running on gasoline. *J Power Sources*. 2019;435:226732.
9. Skinner SJ. Recent advances in the understanding of the evolution of surfaces and interfaces in solid oxide cells. *Adv Mater Interfaces*. 2019;6(15):1900580.
10. Li M, Niu HJ, Druce J, et al. A CO_2-tolerant perovskite oxide with high oxide ion and electronic conductivity. *Adv Mater*. 2020;32(4):1905200.
11. Wachsman E, Ishihara T, Kilner J. Low-temperature solid-oxide fuel cells. *MRS Bull*. 2014;39(9):773–782.
12. Kilner JA, Burriel M. Materials for intermediate-temperature solid-oxide fuel cells. *Annu Rev Mater Res*. 2014;44(1):365–393.
13. Gao R, Fernandez A, Chakraborty T, et al. Correlating surface crystal orientation and gas kinetics in perovskite oxide electrodes. *Adv Mater*. 2021;33(20):2100977.
14. Dai HL, Da'as EH, Shafi SP, Wang HQ, Bi L. Tailoring cathode composite boosts the performance of proton-conducting SOFCs fabricated by a one-step co-firing method. *J Eur Ceram Soc*. 2018;38(7):2903–2908.
15. Tao SW, Irvine JTS. A stable, easily sintered proton-conducting oxide electrolyte for moderate-temperature fuel cells and electrolyzers. *Adv Mater*. 2006;18(12):1581–1584.
16. Fabbri E, Bi L, Tanaka H, Pergolesi D, Traversa E. Chemically stable Pr and Y Co-doped barium zirconate electrolytes with high proton conductivity for intermediate-temperature solid oxide fuel cells. *Adv Funct Mater*. 2011;21(1):158–166.

17. Bi L, Boulfrad S, Traversa E. Steam electrolysis by solid oxide electrolysis cells (SOECs) with proton-conducting oxides. *Chem Soc Rev*. 2014;43(24):8255–8270.
18. Chen M, Xie XB, Guo JH, Chen DC, Xu Q. Space charge layer effect at the platinum anode/$BaZr_{0.9}Y_{0.1}O_3$ electrolyte interface in proton ceramic fuel cells. *J Mater Chem A*. 2020;8(25):12566–12575.
19. Xu YS, Xu X, Bi L. A high-entropy spinel ceramic oxide as the cathode for proton-conducting solid oxide fuel cells. *J Adv Ceram*. 2022;11(5):794–804.
20. Duan CC, Huang JK, Sullivan N, O'Hayre R. Proton-conducting oxides for energy conversion and storage. *Appl Phys Rev*. 2020;7(1):011314.
21. Guo YM, Lin Y, Ran R, Shao ZP. Zirconium doping effect on the performance of proton-conducting $BaZr_yCe_{0.8-y}Y_{0.2}O_3$ ($0.0 \le y \le 0.8$) for fuel cell applications. *J Power Sources*. 2009;193(2):400–407.
22. Fabbri E, Bi L, Pergolesi D, Traversa E. High-performance composite cathodes with tailored mixed conductivity for intermediate temperature solid oxide fuel cells using proton conducting electrolytes. *Energy Environ Sci*. 2011;4(12):4984–4993.
23. Xu X, Wang HQ, Fronzi M, Wang XF, Bi L, Traversa E. Tailoring cations in a perovskite cathode for proton-conducting solid oxide fuel cells with high performance. *J Mater Chem A*. 2019;7(36):20624–20632.
24. Zhou C, Sunarso J, Song YF, et al. New reduced-temperature ceramic fuel cells with dual-ion conducting electrolyte and triple-conducting double perovskite cathode. *J Mater Chem A*. 2019;7(21):13265–13274.
25. Song YS, Chen YB, Wang W, et al. Self-assembled triple-conducting nanocomposite as a superior protonic ceramic fuel cell cathode. *Joule*. 2019;3(11):2842–2853.
26. Tong XF, Xu X, Tripkovic D, Hendriksen PV, Kiebach WR, Chen M. Promotion of oxygen reduction and evolution by applying a nanoengineered hybrid catalyst on cobalt free electrodes for solid oxide cells. *J Mater Chem A*. 2020;8(18):9039–9048.
27. Yamaura H, Ikuta T, Yahiro H, Okada G. Cathodic polarization of strontium-doped lanthanum ferrite in proton-conducting solid oxide fuel cell. *Solid State Ionics*. 2005;176(3-4):269–274.
28. Xu X, Xu YS, Ma JM, et al. Tailoring electronic structure of perovskite cathode for proton-conducting solid oxide fuel cells with high performance. *J Power Sources*. 2021;489:229486.
29. Xu X, Wang HQ, Ma JM, et al. Impressive performance of proton-conducting solid oxide fuel cells using a first-generation cathode with tailored cations. *J Mater Chem A*. 2019;7(32):18792–18798.
30. Ren RZ, Wang ZH, Meng XG, et al. Tailoring the oxygen vacancy to achieve fast intrinsic proton transport in a perovskite cathode for protonic ceramic fuel cells. *Acs Appl Energy Mater*. 2020;3(5):4914–4922.
31. Porras-Vazquez JM, Slater PR. Synthesis and characterization of oxyanion-doped cobalt containing perovskites. *Fuel Cells*. 2012;12(6):1056–1063.
32. Gao JT, Li Q, Zhang ZP, Lu Z, Wei B. A cobalt-free bismuth ferrite-based cathode for intermediate temperature solid oxide fuel cells. *Electrochem Commun*. 2021;125:106978.
33. Zhang XH, Pei CL, Chang X, et al. FeO_6 octahedral distortion activates lattice oxygen in perovskite ferrite for methane partial oxidation coupled with CO_2 splitting. *J Am Chem Soc*. 2020;142(26):11540–11549.
34. Xu YS, Liu XH, Cao N, Xu X, Bi L. Defect engineering for electrocatalytic nitrogen reduction reaction at ambient conditions. *Sustain Mater Technol*. 2021;27:e00229.
35. Yin YR, Yu SF, Dai HL, Bi L. Triggering interfacial activity of the traditional La0.5Sr0.5MnO3 cathode with Co-doping for proton-conducting solid oxide fuel cells. *J Mater Chem A*. 2022;10(4):1726–1734.
36. Tao ZR, Xu X, Bi L. Density functional theory calculations for cathode materials of proton-conducting solid oxide fuel cells: a mini-review. *Electrochem Commun*. 2021;129:107072.
37. Saranya AM, Pla D, Morata A, et al. Engineering mixed ionic electronic conduction in $La_{0.8}Sr_{0.2}MnO_3$ nanostructures through fast grain boundary oxygen diffusivity. *Adv Energy Mater*. 2015;5(11):1500377.
38. Ji QQ, Bi L, Zhang JT, Cao HJ, Zhao XS. The role of oxygen vacancies of ABO_3 perovskite oxides in the oxygen reduction reaction. *Energy Environ Sci*. 2020;13(5):1408–1428.
39. Xie Y, Shi N, Huan DM, et al. A stable and efficient cathode for fluorine-containing proton-conducting solid oxide fuel cells. *ChemSusChem*. 2018;11(19):3423–3430.
40. Xu YS, Xu X, Cao N, et al. Perovskite ceramic oxide as an efficient electrocatalyst for nitrogen fixation. *Int J Hydrog Energy*. 2021;46(17):10293–10302.
41. Wu S, Xu X, Li XM, Bi L. High-performance proton-conducting solid oxide fuel cells using the first-generation Sr-doped $LaMnO_3$ cathode tailored with Zn ions. *Sci China Mater*. 2022;65(3):675–682.
42. Lu XK, Yang X, Jia LC, Chi B, Pu J, Li J. First principles study on the oxygen reduction reaction of the $La_{1-x}Sr_xMnO_3$ coated $Ba_{1-x}Sr_xCo_{1-y}Fe_yO_3$ cathode for solid oxide fuel cells. *Int J Hydrog Energy*. 2019;44(31):16359–16367.
43. Lin L, Xu Q, Wang YP, et al. Property optimization for strontium-rich lanthanum chromium ferrite cathodes: a demonstration of lanthanide replacement effect. *Mater Res Bull*. 2018;106:263–270.
44. Fan TW, Wang ZP, Lin JJ, et al. First-principles predictions for stabilizations of multilayer nanotwins in Al alloys at finite temperatures. *J Alloy Compd*. 2019;783:765–771.
45. Zhang LL, Yin YR, Xu YS, Yu SF, Bi L. Tailoring $Sr_2Fe_{1.5}Mo_{0.5}O_6$ with Sc as a new single-phase cathode for proton-conducting solid oxide fuel cells. *Sci China Mater*. 2022;65(6):1485–1494.
46. Chen JY, Zhang W, Li HZ, et al. Recent advances in TiO_2-based catalysts for N_2 reduction reaction. *SusMat*. 2021;1(2):174–193.
47. Li ZS, Lv L, Wang JS, et al. Engineering phosphorus-doped $LaFeO_3$ perovskite oxide as robust bifunctional oxygen electrocatalysts in alkaline solutions. *Nano Energy*. 2018;47:199–209.
48. Suntivich J, May KJ, Gasteiger HA, Goodenough JB, Shao-Horn Y. A perovskite oxide optimized for oxygen evolution catalysis from molecular orbital principles. *Science*. 2011;334(6061):1383–1385.
49. Peng RR, Wu TZ, Liu W, Liu XQ, Meng GY. Cathode processes and materials for solid oxide fuel cells with proton conductors as electrolytes. *J Mater Chem*. 2010;20(30):6218–6225.
50. Bi L, Zhang SQ, Fang SM, Tao ZT, Peng RR, Liu W. A novel anode supported $BaCe_{0.7}Ta_{0.1}Y_{0.2}O_3$ electrolyte membrane for proton-conducting solid oxide fuel cell. *Electrochem Commun*. 2008;10(10):1598–1601.

51. Ding HP, Lin B, Liu XQ, Meng GY. High performance protonic ceramic membrane fuel cells (PCMFCs) with $Ba_{0.5}Sr_{0.5}Zn_{0.2}Fe_{0.8}O_3$ perovskite cathode. *Electrochem Commun*. 2008;10(9):1388–1391.
52. Tao ZT, Bi L, Zhu ZW, Liu W. Novel cobalt-free cathode materials $BaCe_xFe_{1-x}O_3$ for proton-conducting solid oxide fuel cells. *J Power Sources*. 2009;194(2):801–804.
53. Ling YH, Zhang XZ, Wang SL, Zhao L, Lin B, Liu XQ. A cobalt-free $SrFe_{0.9}Sb_{0.1}O_3$ cathode material for proton-conducting solid oxide fuel cells with stable $BaZr_{0.1}Ce_{0.7}Y_{0.1}Yb_{0.1}O_3$ electrolyte. *J Power Sources*. 2010;195(20):7042–7045.
54. Zhao L, He BB, Ling YH, et al. Cobalt-free oxide $Ba_{0.5}Sr_{0.5}Fe_{0.8}Cu_{0.2}O_3$ for proton-conducting solid oxide fuel cell cathode. *Int J Hydrog Energy*. 2010;35(8):3769–3774.
55. Ling YH, Yu J, Lin B, Zhang XZ, Zhao L, Liu XQ. A cobalt-free $Sm_{0.5}Sr_{0.5}F_{e0.8}Cu_{0.2}O_3$-$Ce_{0.8}Sm_{0.2}O_2$ composite cathode for proton-conducting solid oxide fuel cells. *J Power Sources*. 2011;196(5):2631–2634.
56. Yan LT, Ding HP, Zhu ZW, Xue XJ. Investigation of cobalt-free perovskite $Ba_{0.95}La_{0.05}FeO_3$ as a cathode for proton-conducting solid oxide fuel cells. *J Power Sources*. 2011;196(22):9352–9355.
57. Yang ZJ, Wang NB, Xiao J, et al. A novel cobalt-free $Ba_{0.5}Sr_{0.5}Fe_{0.9}Mo_{0.1}O_3$-$BaZr_{0.1}Ce_{0.7}Y_{0.2}O_3$ composite cathode for solid oxide fuel cells. *J Power Sources*. 2012;204:89–93.
58. Ding ZL, Yang ZJ, Zhao DM, Deng XL, Ma GL. A cobalt-free perovskite-type $La_{0.6}Sr_{0.4}Fe_{0.9}Cr_{0.1}O_3$ cathode for proton-conducting intermediate temperature solid oxide fuel cells. *J Alloy Compd*. 2013;550:204–208.
59. Yu T, Mao XB, Ma GL. Performance of cobalt-free perovskite $La_{0.6}Sr_{0.4}Fe_{1-x}Nb_xO_3$ cathode materials for proton-conducting IT-SOFC. *J Alloy Compd*. 2014;608:30–34.
60. Ma JM, Tao ZT, Kou HN, Fronzi M, Bi L. Evaluating the effect of Pr-doping on the performance of strontium-doped lanthanum ferrite cathodes for protonic SOFCs. *Ceram Int*. 2020;46(3):4000–4005.
61. Tang HD, Jin ZZ, Wu YS, Liu W, Bi L. Cobalt-free nanofiber cathodes for proton conducting solid oxide fuel cells. *Electrochem Commun*. 2019;100:108–112.
62. Da'as EH, Bi L, Boulfrad S, Traversa E. Nanostructuring the electronic conducting $La_{0.8}Sr_{0.2}MnO_3$ cathode for high-performance in proton-conducting solid oxide fuel cells below 600 degrees C. *Sci China Mater*. 2018;61(1):57–64.
63. Wang Q, Hou J, Fan Y, et al. $Pr_2BaNiMnO_7$ double-layered Ruddlesden–Popper perovskite oxides as efficient cathode electrocatalysts for low temperature proton conducting solid oxide fuel cells. *J Mater Chem A*. 2020;8(16):7704–7712.
64. Chen Y, Yoo S, Pei K, et al. An in situ formed, dual-phase cathode with a highly active catalyst coating for protonic ceramic fuel cells. *Adv Funct Mater*. 2018;28(5):1704907.
65. Tarutin AP, Lyagaeva JG, Medvedev DA, Bi L, Yaremchenko AA. Recent advances in layered Ln_2NiO_4 nickelates: fundamentals and prospects of their applications in protonic ceramic fuel and electrolysis cells. *J Mater Chem A*. 2021;9(1):154–195.
66. Choi S, Kucharczyk CJ, Liang YG, et al. Exceptional power density and stability at intermediate temperatures in protonic ceramic fuel cells. *Nat Energy*. 2018;3(3):202–210.
67. Wang B, Liu XH, Bi L, Zhao XS. Fabrication of high-performance proton-conducting electrolytes from microwave prepared ultrafine powders for solid oxide fuel cells. *J Power Sources*. 2019;412:664–669.
68. Xu X, Bi L, Zhao XS. Highly-conductive proton-conducting electrolyte membranes with a low sintering temperature for solid oxide fuel cells. *J Membr Sci*. 2018;558:17–25.
69. Hohenberg P, Kohn W. Inhomogeneous electron gas. *Phys Rev*. 1964;136(3B):B864.
70. Kresse G, Furthmuller J. Efficient iterative schemes for ab initio total-energy calculations using a plane-wave basis set. *Phys Rev B*. 1996;54(16):11169–11186.
71. Payne MC, Teter MP, Allan DC, Arias T, Joannopoulos JD. Iterative minimization techniques for ab initio total-energy calculations: molecular dynamics and conjugate gradients. *Rev Mod Phys*. 1992;64(4):1045.
72. Kohn W, Sham LJ. Self-consistent equations including exchange and correlation effects. *Phys Rev*. 1965;140(4A):A1133.
73. Dan X, Wang C, Xu X, et al. Improving the sinterability of CeO_2 by using plane-selective nanocubes. *J Eur Ceram Soc*. 2019;39(14):4429–4434.

SUPPORTING INFORMATION

Additional supporting information can be found online in the Supporting Information section at the end of this article.

How to cite this article: Yin Y, Dai H, Yu S, Bi L, Traversa E. Tailoring cobalt-free $La_{0.5}Sr_{0.5}FeO_{3-\delta}$ cathode with a nonmetal cation-doping strategy for high-performance proton-conducting solid oxide fuel cells. *SusMat*. 2022;2:607–616. https://doi.org/10.1002/sus2.79